Supporting Information

Ball-milling-assisted construction of ternary mixed-metal oxide/g-C$_3$N$_4$ heterostructures for synergistic polysulfide adsorption and catalytic conversion in lithium-sulfur batteries

Taehun Jeong[a,†], Jinseok Han[a,†], Xin Dong[b], Rong Yang[b], Ying Liu[a,*], Jinjoo Park[a], Jae-Kwang Kim[a,*]

[a]*Department of Energy Convergence Engineering, Cheongju University, Cheongju 28503, Republic of Korea*

[b]*International Research Center for Composite and Intelligent Manufacturing Technology, Institute of Chemical Power Sources, Xi'an University of Technology, Xi'an 710048, People's*

[†]These two authors contributed equally to this work.

Corresponding author

E-mail address: jaekwang@cju.ac.kr (J.K. Kim)

lying@cju.ac.kr (Y. Liu)

Table S1. A comparison of the specific capacities of Q_H and Q_L, derived from their charge-discharge profiles at a rate of 0.1C

	Q_{H-R} (mAh g^{-1})	Q_{H-R}/Q_{H-T} Ratio (%)	Q_{L-R} (mAh g^{-1})	Q_{H-R}/Q_{H-T} Ratio (%)
HGN@PP	415	99.0%	1042	83.0%
g-C$_3$N$_4$@PP	240	57.3%	904	72.0%
NiCoZn-O@PP	361	86.2%	995	79.2%
PP	305	72.8%	796	63.4%

Note: Q_{H-R}/Q_{L-R} refer to the actual discharge capacity of the upper/lower plateau in the cell; Q_{H-T}/Q_{H-T} refer to the theoretical discharge capacity of the upper/lower plateau in the cell
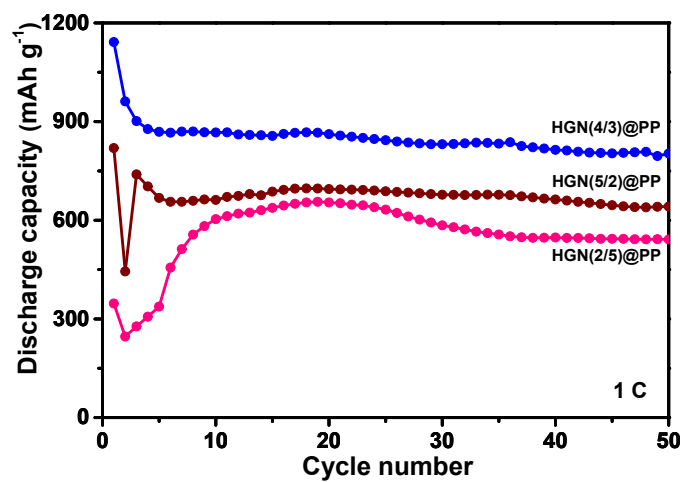
Fig. S1. Cycling performance of Li–S cells employing HGN@PP separators with different g-C$_3$N$_4$/NiCoZn–O mass ratios at 1 C.
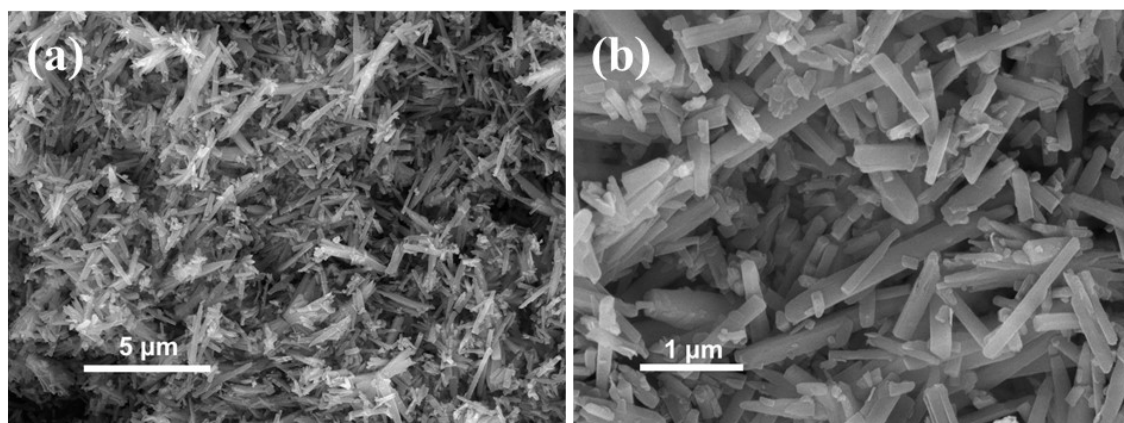
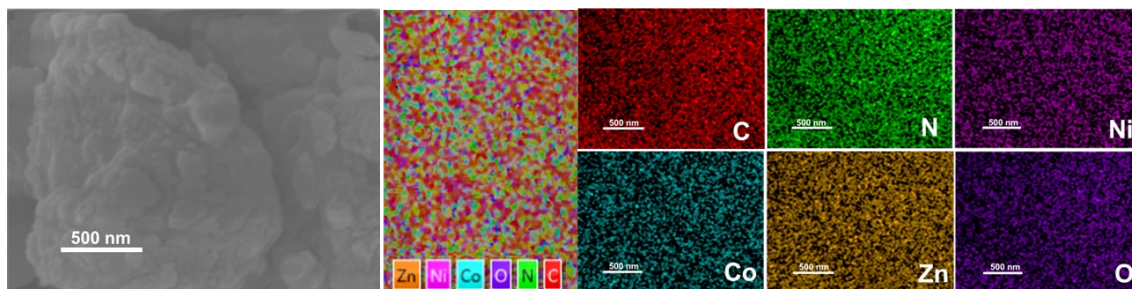**Fig. S2.** FE-SEM images of the synthesized trimetallic MOF.

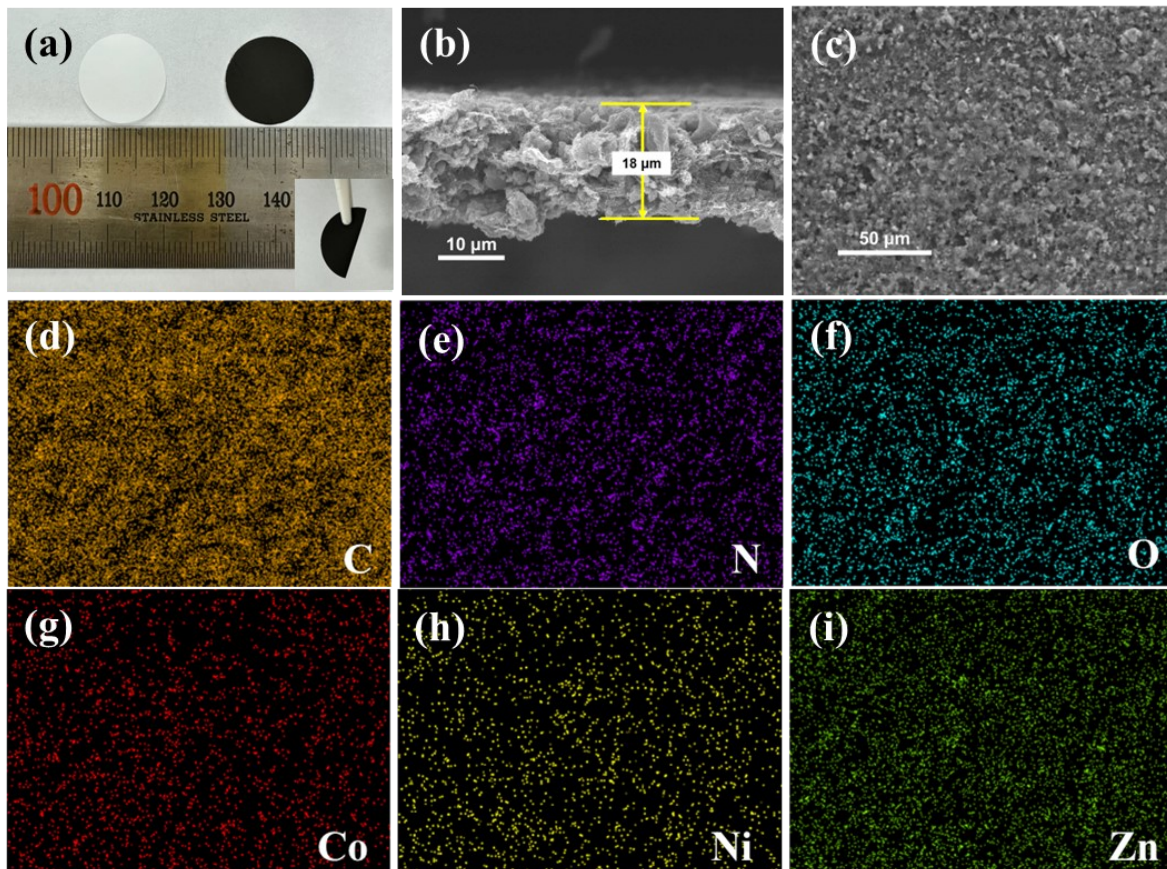**Fig. S3.** FE-SEM image and EDS mapping of HGN composite.

Fig. S4. (a) Digital images of the PP and HGN@PP separators, FE-SEM images of (b) the cross-section of the HGN@PP separator, (c) the surface of the HGN@PP separator, and (d–i) EDS mapping of the HGN@PP separator.
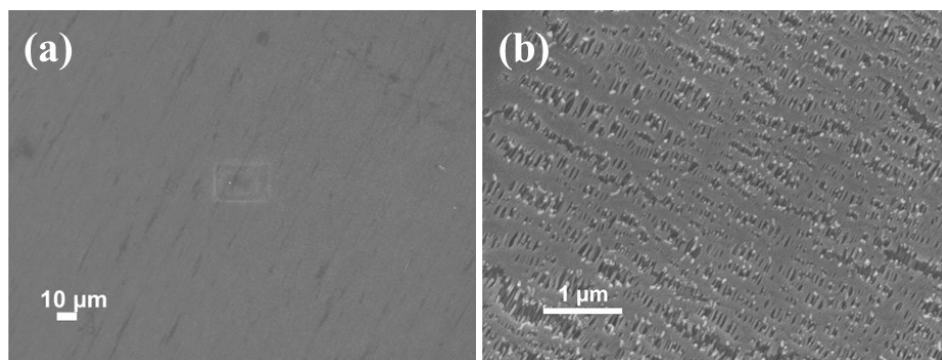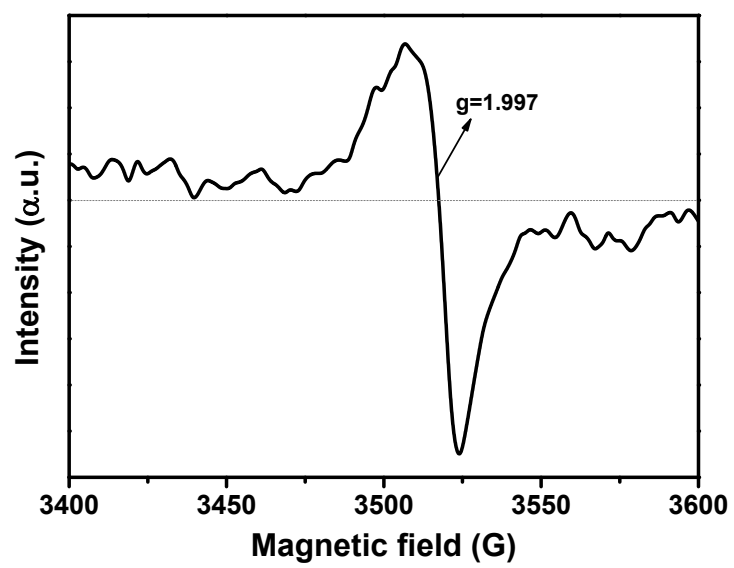
Fig. S5. FE-SEM images of the commercial PP.
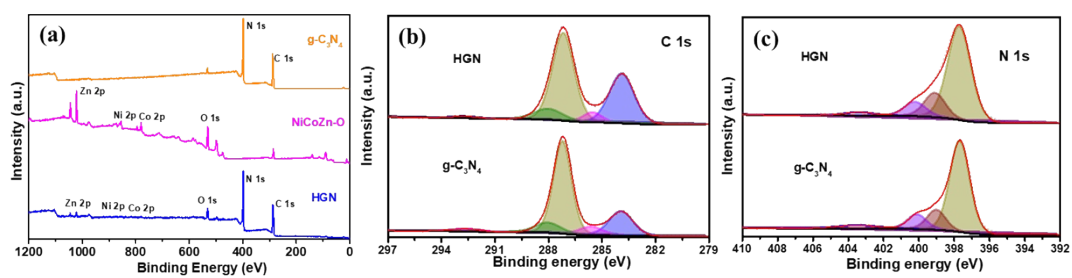
Fig. S6. ERP spectra of HGN composite.

Fig. S7. (a) XPS survey spectra of g-C$_3$N$_4$, NiCoZn-O, and HGN, XPS spectra of (b) C 1s, (c) N 1s of HGN and g-C$_3$N$_4$.

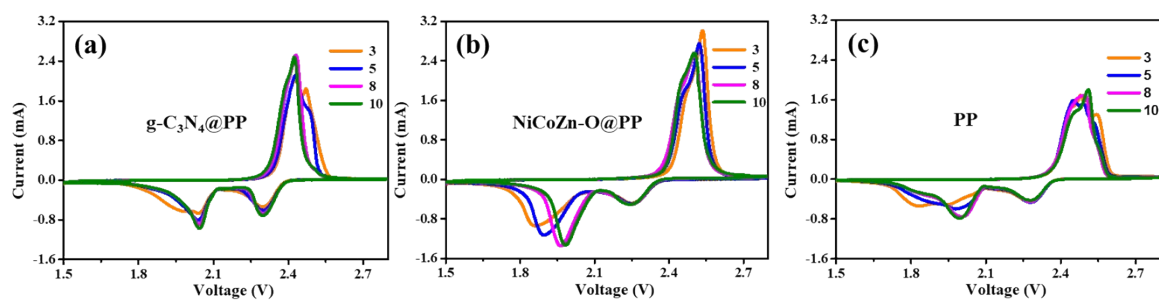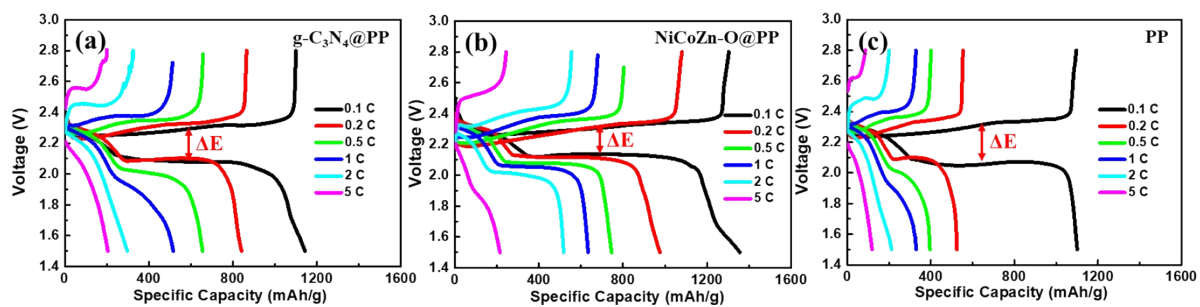**Fig. S8.** CV curves of (a) g-C$_3$N$_4$@PP, (b) NiCoZn-O@PP, (c) PP cells with a scan rate of 0.1 mV s^{-1}.

Fig. S9. First galvanostatic charge–discharge profiles of the cell with (a) g-C$_3$N$_4$@PP, (b) NiCoZn-O@PP, (c) PP cells at different C-rates.
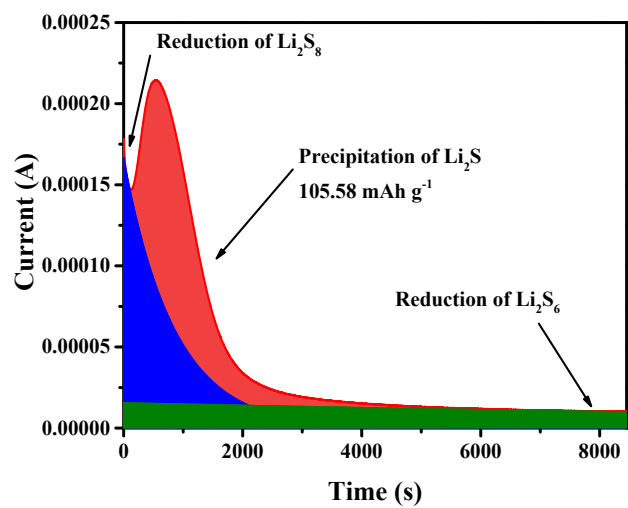
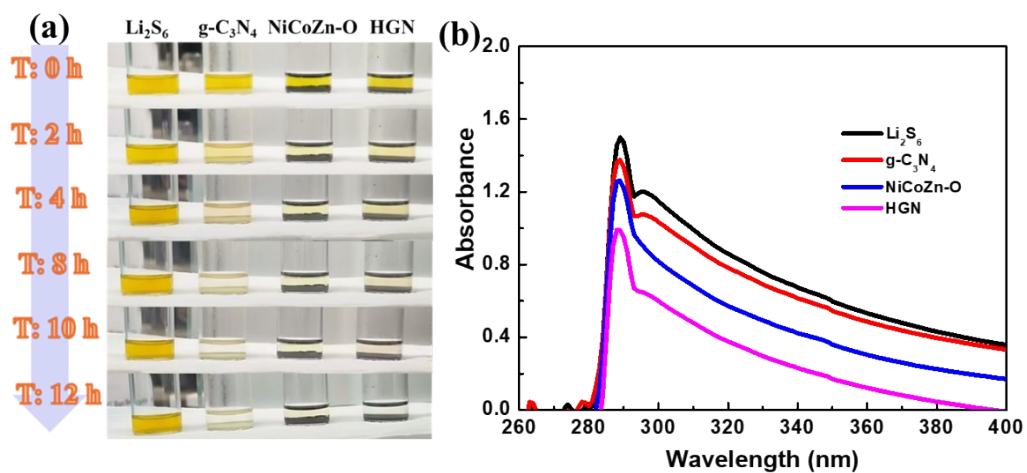**Fig. S10.** Potentiostatic discharge curve of Li_2S_8 tetraglyme solution on the HGN.

Fig. S11. (a) Optical images showing the adsorption of Li_2S_6 solutions by $g\text{-}C_3N_4$, NiCoZn-O, and HGN over a period of 0-12 h, respectively, (b) UV–Vis analysis of the Li_2S_6 solution after adsorption.

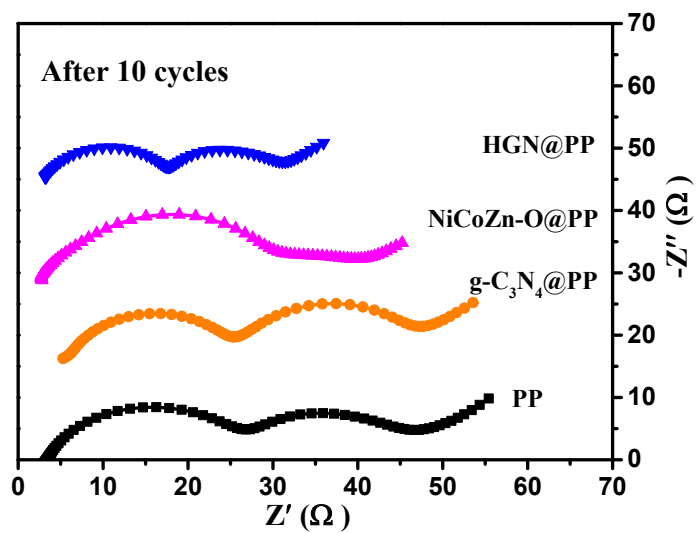**Fig. S12.** EIS spectra of cells with HGN@PP, g-C$_3$N$_4$@PP, NiCoZn-O@PP, and PP separators after cycling.
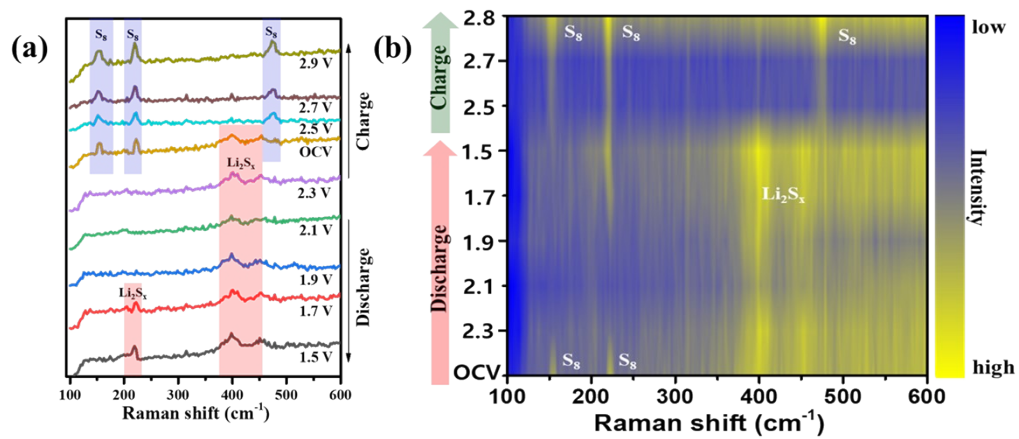
Fig. S13. (a) *in-situ* Raman spectroscopy performed on the anode side of the cell with a PP separator, (b) corresponding Raman contour plot of the charge–discharge process for the cell with a PP separator.